Appendix A

Improvements to the Plasma Current and Electrode Voltage Diagnostics

The plasma current and electrode voltage are extremely important measurements, and this section outlines steps taken to improve both sets of data. The main result is the connection of the grounding clip of the HV probe to the lower electrode and proper attenuation of the voltage signal. These improvements are vital is studying the detachment of the plasma from the electrode in Chapter 4. We also discuss the optoelectric converters that transmit the current and voltage (IV) data, spurious signals due to ground loops, and noise-reduction techniques.

A.1 Optoelectric Modules

The HV probe and Rogowski coil transmit their signals to the DAQ via optoelectric modules [Analog Modules, Inc., Model 732T-2.5-33K-10M]. Each module consists of two devices: a transmitter, which converts an electrical signal into an optical one, and a receiver, which receives the optical signal and converts it back into an electrical one. The transmitter and receiver communicate via a fiber optic cable. The two transmitters, one each for the Rogowski coil and the HV probe, are located by the vacuum chamber and connect their respective probe, while the two receivers are located by the DAQ. The modules transmit frequencies from 10 MHz down to DC. They have a 33 kΩ input resistance and can transmit signals in the range of $\pm$2.5 V; beyond this voltage range, the modules clip the signal.

The optoelectric modules offer several advantages. First, both the HV probe and the Rogowski coil are designed to be read by a high-impedance device such as an oscilloscope. The DAQ, however, has a built-in 50 Ω termination that would distort the probes' signals. For instance, if the Rogowski coil circuit of Fig. 2.6 were terminated in 50 Ω, the integrating capacitor would see its resistor R in parallel with the 50 Ω termination, so the circuit time constant would be $(R \parallel 50\ \Omega)C$. This new

time constant is much shorter than the intended time RC, and the signal would suffer distortion. A similar argument applies to the HV probe. The optoelectric modules therefore act as a buffer circuit; the transmitter input impedance is 33 kΩ, providing both probes with a relatively high impedance, and the receivers, powered by active electronics, can drive the 50 Ω termination of the DAQ that would load the probes. Second, signal transmission via fiber optic cables is less susceptible to noise than transmission via braided coaxial cable. While the modules do introduce some noise, this noise is smaller than that associated with transmitting the signal via braided coaxial cable. Finally, the modules offer electrical isolation as the fiber optic cables do not electrically connect the transmitter and receiver. This prevents the formation of ground loops and allows the use of the HV probe grounding clip, as is discussed next.

A.2 The HV Probe Grounding Clip

The HV probe has a grounding clip relative to which it measures large potential differences. As the HV probe measures the electrode voltage and the probe itself is connected to the upper electrode, the grounding clip should be connected to the lower electrode. However, it had been long-standing practice to leave the grounding clip of the HV probe detached from the lower electrode and not connected to anything. In this configuration, the probe measures the voltage of the upper electrode relative to some unknown floating potential. Ostensibly, the omission of the grounding clip was done to prevent the formation of a ground loop as follows. The lower electrodes are electrically connected to the chamber through the grounding cables of the main capacitor bank; connecting the grounding clip to the lower electrodes would form a second electrical connection to the chamber through the DAQ as discussed in Sec. 3.3.2; this second connection would form a large ground loop spanning the laboratory. However, the grounding clip *can* be safely attached to the lower electrodes because the optoelectric module provide electrical isolation, preventing the second ground loop from forming. Indeed, attaching the grounding clip changed the nature of the voltage signal; Fig. A.1 compares the voltage data with and without the clip in use. The clipping at 1.5 kV is due to the optoelectric module and is avoided by adding a frequency-compensated voltage divider as will be described in Sec. A.4. However, even with the clipping, the difference in the HV probe output with and without the grounding clip is apparent, and the signal with the grounding clip in use is believed to be more accurate.

A.3 Ground Loops and Isolation Transformers

Large spurious signals started appearing in both the IV data, seemingly spontaneously. Ultimately, the source of these signals was traced to a small ground loop formed by the I and V cables at the

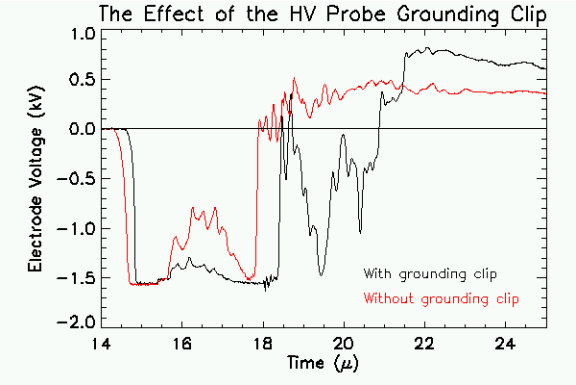

Figure A.1: Use of the HV probe grounding clip on the lower electrode causes significant changes in the signal. Here, the electrode voltage is compared with and without the grounding clip so that the effects of leaving the grounding clip floating can be seen. The clipping is due to the optoelectric modules and will be resolved in Sec. A.4.

DAQ. The cables share a common ground at the DAQ but also at the receiver modules because both modules are powered off the same power supply. To break up the ground loop, a 1:1 isolation transformer was added to the voltage line. However, the low-frequency response of the transformer was quite poor, and to understand this problem we need to look at the equations for a transformer.

Ideally, a 1-1 transformer transmits the signal without distortion or attenuation. From the circuit diagram in Fig. A.2, the voltage loop equations in the left and right circuits are

$$V = i\omega L I_1 - i\omega M I_2 + R_1 I_1, \tag{A.1}$$

$$0 = i\omega L I_2 - i\omega M I_1 + R_2 I_2, \tag{A.2}$$

where M is the mutual inductance of the transformer and is assumed to be nearly equal to L. Ideal operation occurs when we assume $M = L$ and $\omega L \gg R_1 R_2/(R_1 + R_2)$. Defining the difference $\delta I = I_1 - I_2$, Eq. (A.2) becomes $i\omega L \delta I = R_2 I_2$, and Eq. (A.1) becomes

$$V = i\omega L \delta I + R_1 (I_2 + \delta I) \tag{A.3}$$

$$= R_2 I_2 + R_1 I_2 + \frac{R_1 R_2}{i\omega L} I_2 \tag{A.4}$$

$$\approx R_2 I_2 + R_1 I_2. \tag{A.5}$$

It follows that the output voltage, which is the voltage across R_2, is

$$V_{\text{out}} = \frac{R_2}{R_1 + R_2} V, \tag{A.6}$$

which is the equation for a simple voltage divider. In this ideal case, the transformer couples the two circuits so well that the circuit behaves as if the transformer were not present. Moreover,

the internal resistance of the optoelectric module is probably quite small, meaning that $R_1 \approx 0$. hence, the condition for ideal operation, $\omega L \gg R_1 R_2/(R_1 + R_2)$, will almost always be met because $R_1 R_2/(R_1 + R_2) \approx 0$.

However, when $R_2 \geq \omega L \gg R_1 R_2/(R_1 + R_2)$, the optoelectric module becomes severely loaded and cannot provide the current necessary to maintain ideal operation. Let us compute the theoretical output requirement of the module in this regime. We showed that $i\omega L \delta I = R_2 I_2$, so

$$I_1 = \delta I + I_2 = \left(1 + \frac{R_2}{i\omega L}\right) I_2 \approx \left(1 + \frac{R_2}{i\omega L}\right) \frac{V}{R_1 + R_2}, \tag{A.7}$$

where Eq. (A.5) has been used in the last line. I_1 therefore increases as ω decreases below R_2/L. We suspect that the receiver module becomes extremely loaded at low frequencies and cannot provide this theoretical current. To remedy the problem, a 100 Ω resistor was placed in series in the voltage line in between the receiver module and the transformer, effectively changing R_1 from 0 to 100 Ω. This changes the denominator in Eq. (A.7) from 50 Ω to 150 Ω, cutting the current requirement by a factor of three. This is sufficient to relieve loading of the module in the frequency range of interest, and the transformer faithfully transmits the voltage signals. The added 100 Ω resistance forms an effective voltage divider with the 50 Ω of the DAQ, and this voltage attenuation factor of $50/150 = 1/3$ must be incorporated into the voltage signal.

The reason why the ground loop started misbehaving was not identified. The cause may have been a change in the cabling in other diagnostics, particularly the magnetic probes, which had been recently swapped around the time the spurious signals appeared. The magnetic probes contain many cables that could bear large ground currents (see discussion in Sec. 3.3.5) that could couple to the ground loop.

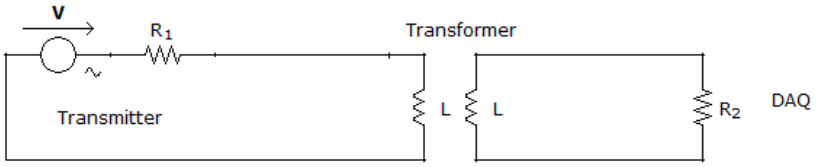

Figure A.2: A circuit diagram for the transmitter module coupled to the DAQ via a 1-1 transformer. The low frequency response of the circuit is poor unless extra resistance is added to R_1.

A.4 HV Probe Termination, Compensation, and Attenuation

The optoelectric modules can only transmit signals up to ±2.5 V, beyond which they clip the signal. The HV probe attenuates the signal by a factor of roughly 923[1], so that a 6 kV electrode voltage is attenuated to about 6 V and would be clipped by the transmitter. To avoid clipping, a simple voltage divider was implemented by placing a 50 kΩ resistor in series with the 33 kΩ input resistance of the transmitter, as shown in Fig. A.3. This provides a theoretical attenuation of $33/(50+33) \approx 0.4$. However, adding this resistance caused the HV probe to integrate the input signal. To understand why, we need to look into the probe's design.

The HV probe has a compensation circuit whose purpose is cancel the effects of stray capacitance across the probe's 10 MΩ and also the oscilloscope's 1 MΩ resistor. By adjusting the components in the compensation circuit, the distortion from the stray capacitance can be minimized such that, for example, a square-wave signal is attenuated without distortion such as rounding the corners (poor high frequency transmission) or drooping (poor low frequency transmission). The compensation circuit is optimized for use with an oscilloscope of 1MΩ impedance and thus is not compatible with different termination impedances such as the 33 kΩ of the transmitter module. To check this experimentally, the probe was terminated in 33 kΩ and given a 100 KHz square-wave input; the square wave was clearly seen to droop as is shown in Fig. A.4.a, indicating less than ideal transmission of low frequencies. This poor low-frequency transmission had always been present in the voltage data even before any of the modifications described here were enacted. However, when the 50 kΩ resistor described above was added, the output changed from less-than-ideal to completely distorted. This is probably because the 50 kΩ resistor combined with both the input capacitance of the optoelectric module and a capacitor in the compensation circuit to form an RC-circuit that integrated the input signal.

To remove this unwanted integration, a small capacitor was added in parallel to the 50 kΩ resistor, as shown in Fig. A.3. This trick is exploited in oscilloscope probes. Consider the circuit in Fig. A.5; and let the complex impedances Z_1 and Z_2 be the parallel combination of R_1 and C_1 and the parallel combination of R_2 and C_2 respectively:

$$Z_1 = \frac{R_1}{1+i\omega R_1 C_1}, \tag{A.8}$$

$$Z_2 = \frac{R_2}{1+i\omega R_2 C_2}. \tag{A.9}$$

If $R_1C_1 = R_2C_2$, then it is seen that Z_1 and Z_2 are proportional to each other with the proportion-

[1]This calibration was done independently by Deepak Kumar and Mark Kendall

ality constant $Z_1/Z_2 = R_1/R_2$. The output voltage, measured across R_2, is then

$$V_{\text{out}} = \frac{Z_2}{Z_1 + Z_2} V_{\text{in}} = \frac{R_2}{R_1 + R_2} V_{\text{in}}, \tag{A.10}$$

which is the equation for a simple voltage divider. When $R_1 C_1 = R_2 C_2$, the effects of the capacitors cancel each other in the output. Indeed, when a 7 pF capacitor was added across the 50 kΩ resistor, the HV probe attenuated square-wave inputs more accurately than had previously been achieved with the probe going straight into the module as shown in Fig A.4.b. The value of 7 pF was determined by trial and error and can, perhaps, be improved.

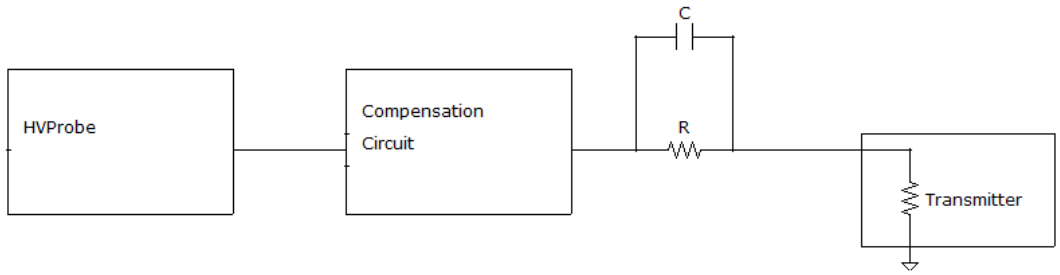

Figure A.3: A resistor R is inserted between the HV probe and the transmitter module creates a voltage divider to avoid signal clipping. The capacitor C is needed for frequency compensation.

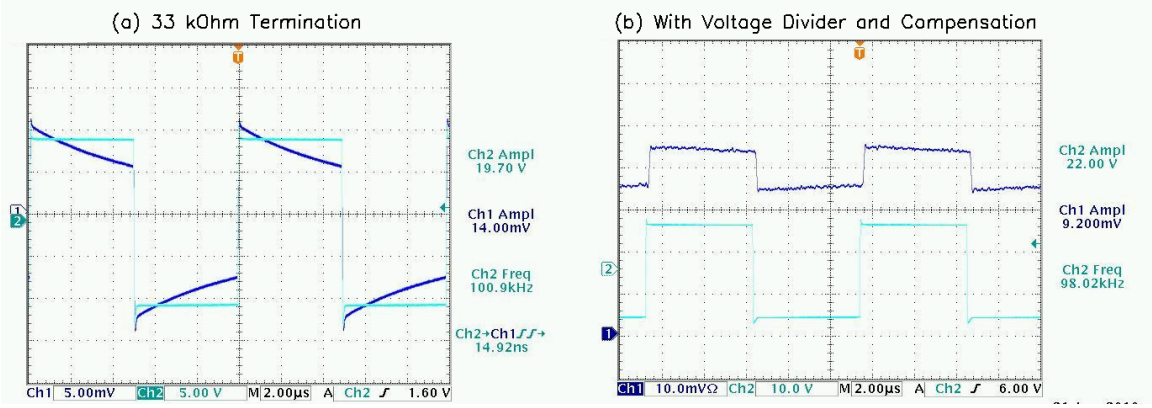

Figure A.4: (a) The HV probe output given a 100 kHz square-wave input when the probe is terminated in 33 kΩ. The output is seen to droop, indicated poor low-frequency response. This distortion had always been present in the signal before any of the modifications outlined here were enacted; however, adding the 50 kΩ resistor shown in Fig. A.3 without the compensating capacitor produced far worse distortion. (b) The probe's output once the 50 kΩ resistor *and* its compensating capacitor have been added. The signal is attenuated by the appropriate amount, and the frequency response is actually a little better than in (a).

Finally, both the 50 kΩ resistor and 7 pF capacitor are soldered directly into the HV probe's compensation circuit box rather than being placed in a separate electrical box in between the com-

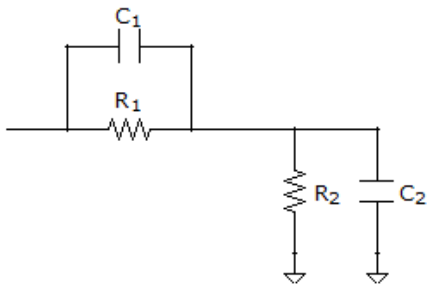

Figure A.5: Given R_2, C_2, and R_1, C_1 can be chosen so that the capacitive effects vanish in the output voltage. The output, as measured across R_2, is then frequency-independent.

pensation circuit and the transmitter. This was done because using a separate box caused arcing at the transmitter due to the large potential difference between the HV probe cable, which is connected to the lower electrode, and the chamber frame on which the transmitter rests. This is not a problem when the HV probe connected directly to the module because the probe is equipped with a high voltage connector. Thus, this arcing is avoided by placing the extra resistor and capacitor inside the compensation circuit.

A.5 Reducing Noise

Some of the modification described so far introduced extra noise into the signals. The isolation transformer added to the voltage signal line introduced high-frequency noise. The attachment of the grounding clip to the lower electrode exascerbated oscillations in the current data that occur at the beginning and middle of the shot. This section describes several attempts to reduce these unwanted side-effects.

Noise reduction in both the IV signals was achieved by moving the receiver modules closer to the DAQ and using shorter lengths of cable to transmit the signals. In general, braided coaxial cable are susceptible to high-frequency noise via transfer impedance as discussed in Sec. 3.3.3, and using less cable sometimes results in less noise. Another possible reason for the noise reduction is that the IV cables were moved further away from the large bundle of cables for the spheromak magnetic probe array, which is suspected to carry large ground currents. Whatever the reason, this relocation mollified the high frequency noise on the voltage traces. The current data improved as well, although this improvement may be due to the added ferrite cores, discussed below.

Large oscillations of about 1 - 2 MHz in the current data are mitigated by the use of ferrite cores. For instance, a ferrite core placed on the HV probe cable offers significant oscillation reduction. Connecting the grounding clip to the lower electrodes connects the local ground of the transmitter

modules; the Rogowski coil ground is also connected to the lower electrodes. We believe that the increased oscillation amplitude on the Rogowski coil is related to sudden changes in the lower electrode voltage which suddenly change the coil ground. The added ferrite around the HV cable makes the connection between the Rogowki coil ground and the lower electrodes high impedance and hence reduces the degree of coupling between lower electrode voltage and transmitter ground voltage. We note that powering the transmitters module with different power supplies could completely isolate the two diagnostics and reduce the oscillations; however, oscillations are still present even when the HV probe is completely detached. Also, adding a ferrite core around the current signal line between the receiver and the DAQ results in modest noise reduction, although the reason for this is not clear.

The remaining oscillations on the current data are probably caused by electrostatic coupling of the Rogowski coil to the main capacitor. The coil sits on top of a copper plate bolted to the capacitor; when the capacitor fires, the voltage of the plate changes drastically, which could induce charge flow on the Rogowski coil [114]. These oscillations are seen at the beginning of the experiment when the voltage is switched on and in the middle of the experiment when the plasma detaches. Indeed, changing the length of braided cable between the coil and the integrating circuit changed the nature of these oscillations. Using a shorter length of cable to connect the coil to the integrating circuit increased the oscillation frequency, presumably because of the reduced stray capacitance of the cable. However, additional spurious signals simultaneously appeared, probably because the integrating circuit was significantly closer to the main capacitor. For the time being, the best place for the integrating circuit appears to be at the transmitter module. To eliminate the oscillation, a shield might be added to the Rogowski coil as per Ref. [114].

Appendix B

Magnetic Scattering of Charged Particles

The vacuum photodiodes described in Chapter 3 utilize permanent magnets to deflect charged particles from the array's interior. In this section, we determine how effectively such magnets shield the array and what particle energies would be required to penetrate through the magnetic field to the detectors. We consider two regimes: the first applies when the particle remains far enough away from the magnet so that the field can be approximated as a pure dipole field. One can then calculate a forbidden region into which particles cannot enter, and the dimensions of this forbidden region measure the deflecting capabilities of the magnet. From these calculations, we determine that electrons are deflected by the magnets but that ions penetrate close to the magnet where the dipole approximation fails. This latter case constitutes the second regime, and we derive a simple formula relating direct measurements of the field close to the magnet to the deflective power of the magnetic geometry.

B.1 The Stormer Region

At large distances from a magnet, the field approximates that of a pure dipole. Particle motion in a dipole field is an old problem first considered by Stormer [115], who established the existence of forbidden regions into which particles of particular energies cannot enter. This region, commonly called the Stormer region, offers an easy criteria for deciding whether or not a particle can enter the detector. The analysis can be extended to other axisymmetric multipole fields [116] and has even been considered for shielding spacecraft [117].

Stormer regions arise through conservation of both kinetic energy and canonical angular momentum. The expression for canonical angular momentum comes from the Lagrangian for a particle in

a magnetic field:

$$\begin{aligned} L &= \frac{m}{2}\mathbf{v}^2 + q\mathbf{v}\cdot\mathbf{A} && \text{(B.1)} \\ &= \frac{m}{2}\left(\dot{\rho}^2 + \rho^2\dot{\phi}^2 + \dot{z}^2\right) + q\left(\dot{\rho}A_\rho + \rho\dot{\phi}A_\phi + \dot{z}A_z\right), && \text{(B.2)} \\ P_\phi &= \frac{\partial L}{\partial\dot{\phi}} = m\rho^2\dot{\phi} + q\rho A_\phi, && \text{(B.3)} \end{aligned}$$

where (ρ, ϕ, z) form a cylindrical coordinate system. An ideal magnetic dipole $\mathbf{m} = m_d\hat{z}$ has a vector potential

$$\mathbf{A} = \frac{\mu_0}{4\pi}\frac{\mathbf{m}\times\hat{r}}{r^3} = \frac{\mu_0 m_d}{4\pi}\frac{\rho}{(\rho^2+z^2)^{3/2}}\hat{\phi}, \tag{B.4}$$

where r is the spherical radius, $r^2 = \rho^2 + z^2$. By azimuthal symmetry, P_ϕ is conserved. Eqs. (B.3) and (B.4) allow us to express the kinetic energy of ϕ motion as a function of position:

$$\frac{m}{2}v_\phi^2 = \frac{m}{2}\rho^2\dot{\phi}^2 = \frac{1}{2m}\left(\frac{P_\phi}{\rho} - q\frac{\mu_0 m_d}{4\pi}\frac{\rho}{(\rho^2+z^2)^{3/2}}\right)^2. \tag{B.5}$$

For a particle moving in a time-independent magnetic field, kinetic energy is also conserved. Of course, the particle's ϕ kinetic energy can never exceed the total kinetic energy, so those spatial locations where Eq. (B.5) predicts an energy greater than $(m/2)v^2$ are forbidden to the particle. It thus follows that the boundary of the forbidden region is where Eq. (B.5) equals $(m/2)v^2$, or

$$\frac{m}{2}v^2 = \frac{1}{2m}\left(\frac{P_\phi}{\rho} - q\frac{\mu_0 m_d}{4\pi}\frac{\rho}{(\rho^2+z^2)^{3/2}}\right)^2. \tag{B.6}$$

Dividing Eq. (B.6) by $(m/2)v^2$ gives

$$1 = \left(\frac{P_\phi}{mv\rho} - \frac{q\mu_0 m_d}{4\pi mv}\frac{\rho}{(\rho^2+z^2)^{3/2}}\right)^2. \tag{B.7}$$

The coefficient of the second terms has the units of length squared and defines the Stormer length C as

$$C := \sqrt{\frac{q\mu_0 m_d}{4\pi mv}}. \tag{B.8}$$

We normalize length by C so that

$$1 = \left(\frac{P_\phi/mvC}{\rho} - \frac{\rho}{(\rho^2+z^2)^{3/2}}\right)^2. \tag{B.9}$$

The size of the forbidden region thus depends on the dimensionless parameter P_ϕ/mvC, which we

shall call k. We can solve Eq. (B.9) for z as a function of ρ,

$$\pm 1 = \frac{k}{\rho} - \frac{\rho}{(\rho^2+z^2)^{3/2}}, \tag{B.10}$$

$$\frac{\rho}{(\rho^2+z^2)^{3/2}} = \frac{k}{\rho} \mp 1, \tag{B.11}$$

$$(\rho^2+z^2)^{3/2} = \frac{\rho^2}{k \mp \rho}, \tag{B.12}$$

$$z^2 = \left(\frac{\rho^2}{k \mp \rho}\right)^{2/3} - \rho^2. \tag{B.13}$$

There are two curves: an upper curve and a lower curve given by the minus sign and the plus sign in Eq. (B.13 respectively. We plot these curves for several value of the parameter k in Fig. B.1, which shows that the lower curve defines a toroidal forbidden region for all k whereas the upper curve undergoes a morphological change at $k = 2$. We will discuss each region in turn.

We first analyze the lower curve, which defines a toroidal forbidden region. The $k \to 0$ case corresponds to particle trajectories with vanishingly small value of canonical angular momentum; these trajectories can be considered "head-on" such that the particle is aimed directly at the collimator with $\dot{\phi}(t=0) \approx 0$[1]. For such trajectories, the upper curve, to be discussed below, is vanishingly small, and the only forbidden region is that defined by the lower curve, as shown in Fig. B.1.a. The size of this region is set by C alone, as can be seen by setting $P_\phi = 0$ in Eq. (B.6). The height of this toroidal region is $0.17C$ and the radial extent is C. Therefore, if $0.17C$ is greater than or equal to the diameter of the collimator, the toroidal regions will deflect head-on trajectories aimed at the collimator.

However, as k increases, the toroidal region shrinks, as can be seen graphically in Fig. B.1. Analytically, the lower curve has precisely one root, which defines the radial extend of the forbidden region:

$$\rho_{\max} = \frac{\sqrt{k^2+4} - k}{2}. \tag{B.14}$$

$\rho_{\max}$ approaches $\rho = 0$ as k increases, confirming that the toroidal region diminishes with increasing angular momentum. Fig. B.2 plots the height and radial extent of the toroidal region as a function of k. From this analysis, one might conclude that particles of non-zero angular momentum could pass the magnet even when $0.17C$ is greater than or equal to the diameter of the collimator. However, we shall now show that the second forbidden region, defined by the upper curve, will deflect such particles for larger k.

The second forbidden region vanishes for small k but grows in extent for larger k, eventually enveloping the toroidal region considered above and defining a very large forbidden region. For

[1] By Eq. (B.3), the condition $\dot{\phi}(t=0) = 0$ does not mean that P_ϕ vanishes but rather $P_\phi = q\mu_0 m_d/4\pi\rho_0$. However, we assume that such "head-on" particle begins at sufficiently large ρ_0 that P_ϕ can be taken to be zero.

$k < 2$, the upper curve has no roots but instead has a singularity at $\rho = k$, so the upper forbidden region is topologically conical as suggested by Fig. B.1.b. This singularity also defines the radial extend of the upper region, which then clearly grows as k increases. As $k \to 2$, the upper curve begins to dip down and eventually meets the $z = 0$ plane as shown in Fig. B.1.c. For $k > 2$, the forbidden region is cylindrical and shaped like an hourglass; additionally, there is a hollow torus inside, as shown in Fig. B.1.d. This hollow space between the upper and lower regions can confine particles in the dipole field, and such trajectories are of particular interest to geophysicists, but this region in accessible to the trajectories considered here which begin far away from the magnets. We note that the upper curve has two roots when $k > 2$:

$$\rho = \frac{k \pm \sqrt{k^2 - 4}}{2}. \tag{B.15}$$

The $-$ sign is the radial extend of the hollow region while the $+$ sign is the minimum radius of the cylindrical forbidden region (e.g. the narrowest radius of the hourglass). When this latter quantity is equal to or larger than the radius of the collimator, the cylindrical region protects the detector from the charged particle. Since $(k + \sqrt{k^2 - 4})/2 \geq 1$, this minimum radius of the cylindrical region is greater than or equal to the Stormer length C.

We thus conclude that particles with a Stormer length $0.17C$ greater than or equal to the collimator radius will most likely be deflected regardless of the particle's canonical angular momentum. For small values of k, the particle is deflected by the toroidal region, and for large k the particle is instead deflected by the cylindrical forbidden region. Fig. B.2 plots the size of both the toroidal and cylindrical region as a function of k and clearly shows this transition for $k > 2$. We acknowledge that, even if $0.17C$ is nearly equal to the collimator radius, a small population of particles may have initial conditions such that the forbidden region is slightly smaller than the collimator radius, and these particles could in principle slip past the magnets. However, we also note that such particles may still acquire some degree of angular deflection and may subsequently crash into the collimator wall after passing the magnetic. Thus, we will still use the Stormer length as the appropriate scale in determining whether a particle is deflected or not.

B.2 Estimates of the Dipole Moment

To compute the Stormer length, we need an estimate of the dipole moment of the deflector magnets. This is estimated both analytically and experimentally; the two results agree well enough to proceed with order-of-magnitude calculations.

The data sheets for the magnets do not give the dipole moment but instead provide the remanence field B_r, which is the field left in the magnet after the external magnetizing field is removed. Ideally,

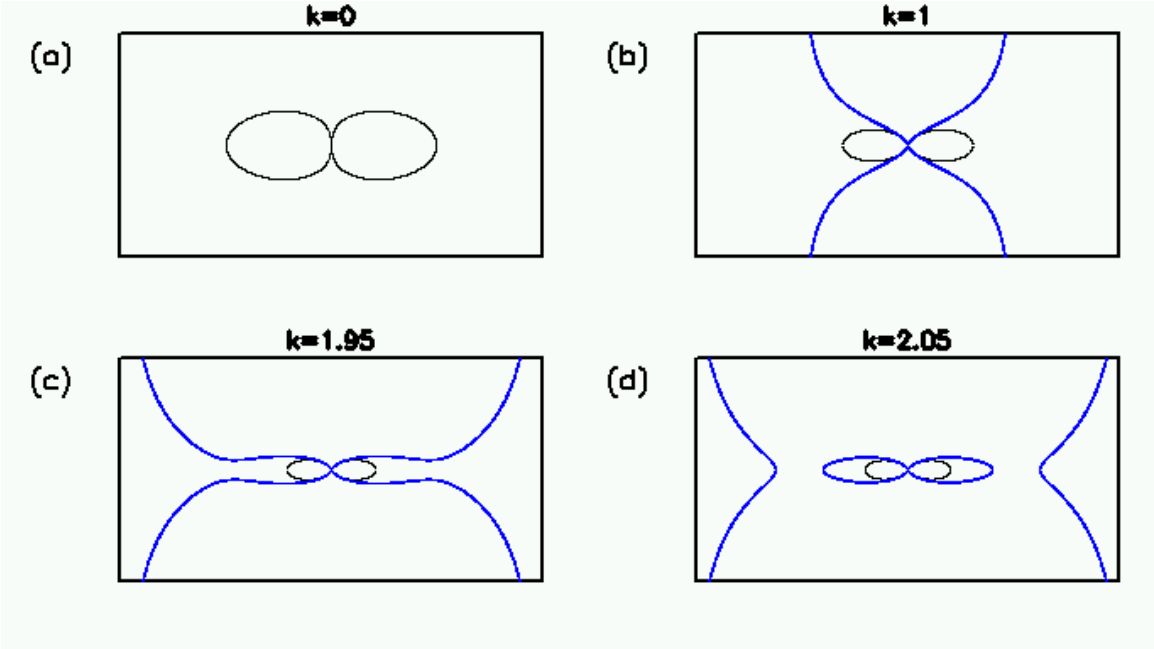

Figure B.1: The forbidden regions plotted for different values of k. (a) At $k = 0$, the upper curve is essentially non-existent, leaving only a toroidal forbidden region. (b) For $0 < k < 2$, the upper curve becomes apparent a defines a cylindrical forbidden region while the toroidal regions diminishes in size. (c) As $k \to 2$, the upper curve begins to bend down towards the $z = 0$ plane. (d) For $k > 2$, the upper curve forms a large cylindrical forbidden region that encloses the smaller toroidal region.

this remanence field is uniform, axial, and of constant strength B_r inside the magnet. Such a field is equivalent to that of an infinite solenoid, and we therefore estimate the dipole moment by treating the magnet like a solenoid. To produce an interior field of strength B_r, the linear current density would have to be $\lambda = B_r/\mu_0$. The magnetic dipole moment density per unit length is then λ times the magnet's area πR^2, and the total dipole moment is

$$m_d = \lambda(\pi R^2)h = \frac{B_r}{\mu_0}\text{Vol}, \tag{B.16}$$

where Vol is the volume of the magnet. This formula implies a magnetization $\mathbf{M} = \mathbf{B}_r/\mu_0$. Indeed, for a uniformly magnetized sphere, the dipole moment is proportional to the product of the interior magnetic field times the sphere's volume [98, pg. 264], although in the case of a sphere there is an additional multiplicative factor due to the different geometry. The magnets originally used on the vacuum photodiodes were neodymium disks of radius $R = 0.75$ cm and height $h = 0.30$ cm and remanence field $B_r = 0.68$ T. This gives an estimated dipole moment of

$$m_d = 0.287 \text{ Am}^2. \tag{B.17}$$

To validate Eq. (B.17), the on-axis field of several disk magnets was measured using a 5100

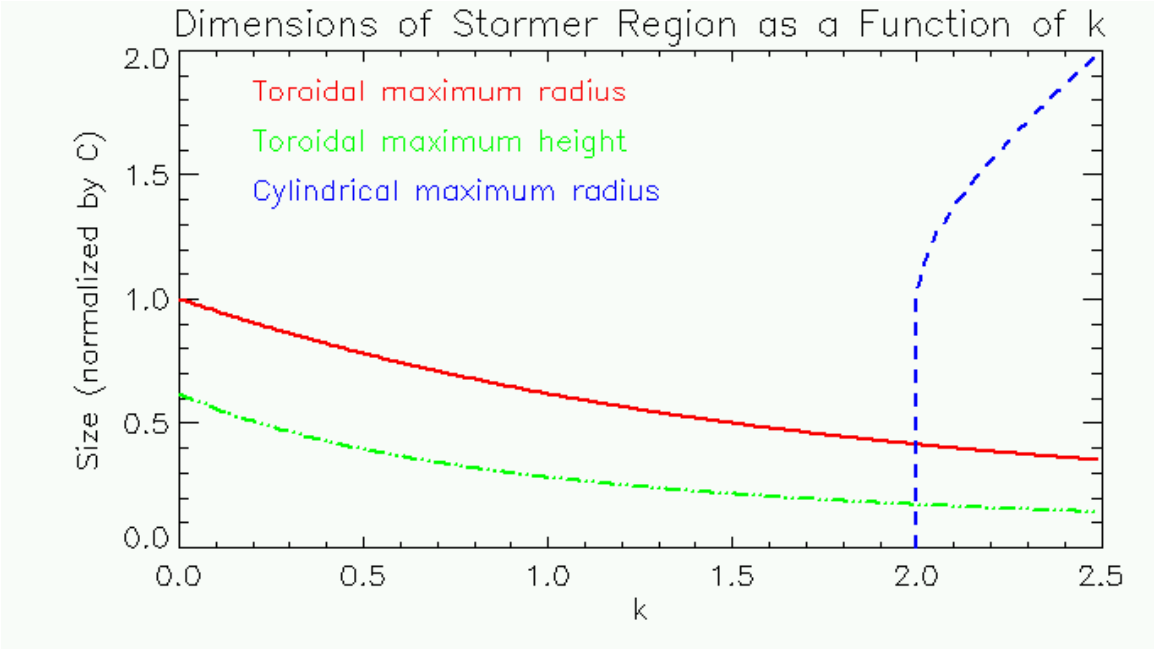

Figure B.2: The spatial extend of the forbidden regions as a function of k. We see that even though the toroidal region diminishes both in radial extent and in height, the larger cylindrical region forms at $k = 2$ and continues to deflect particles as the toroidal region continues to shrink for large k.

Series Gauss meter from F.W. Bell for various heights above the magnet. The height measurements are accurate to within ±2 mm. At every height, the magnet was placed both face up and face down. Subtracting the two values and dividing by two then removes any offsets due to Earth or lab fields. The measurements were done on two of the disk magnets described above. Additionally, a third magnet was measured to check the scaling of magnetic moment with volume; this magnet had $R = 0.75$ cm and height of $h = 0.50$ cm.

We fit the measured magnetic field with the analytical formula for a dipole field. The magnetic field of a pure dipole is

$$\mathbf{B} = \frac{\mu_0 m_d}{4\pi} \frac{2\cos\theta\hat{r} - \sin\theta\hat{\theta}}{r^3}, \tag{B.18}$$

which means that its on-axis value is

$$\mathbf{B}(\rho = 0) = \frac{\mu_0 m_d}{2\pi} \frac{1}{z^3}\hat{z}. \tag{B.19}$$

In principle, $z^3 \cdot B(z)$ should be constant and proportional to the dipole moment. This is not observed in the actual data, indicating that $\mathbf{B}$ is not a pure dipole field but weakens as one approaches the magnet. An octupole multipole moment is therefore added to the fit[2]. We write the octupole field

[2] A quadrupole moment does not obey the symmetry of a disk magnet.

as

$$\mathbf{B}_{\rm oct} = -\nabla\left(m_o\frac{\mu_0}{4\pi}\frac{P_3(\cos\theta)}{r^4}\right) \tag{B.20}$$

$$= -m_o\frac{\mu_0}{4\pi}\left(-4\frac{P_3(\cos\theta)}{r^5}\hat{r} - \sin\theta\frac{P_3'(\cos\theta)}{r^4}\hat{\theta}\right). \tag{B.21}$$

For on-axis measurements, $\theta = 0$. The $\hat{\theta}$ component vanishes, and for all Legendre polynomials, $P_n(1) = 1$, so

$$B_{\rm oct}(\rho) = \frac{\mu_0 m_o}{\pi}\frac{1}{z^5}\hat{z}. \tag{B.22}$$

When this octupole field is added to the dipole field, our analytic formula is

$$B(z) = \frac{\mu_0 m_d}{2\pi}\frac{1}{z^3} + \frac{\mu_0 m_o}{\pi}\frac{1}{z^5}. \tag{B.23}$$

The resulting fit gives a dipole moment of $m_d = 0.2275 \pm 0.0031$ Am^2 and an octupole moment of $m_o = (-1.371 \pm 0.15)\cdot 10^{-5}$ Am^4 for the first of the 5902K61 magnets and $m_d = 0.2292 \pm 0.0031$ Am^2 and $m_o = (-1.4034 \pm 0.15)\cdot 10^{-5}$ Am^4 for the second. The χ^2 values for these fits are 1.15 and 1.19, indicating a good fit. The analytical estimate of the dipole moment given by Eq. (B.17) is thus fair but too large; the discrepancy might be due imperfect magnetization or the approximate nature of the analytical estimate. The octupole moments determined by the fits tells us how the field deviates from a pure dipole field; the distance at which the octupole field strength equals the dipole field is 1.1 cm. If a particle's Stormer length is much larger than 1.1 cm, then we can safely ignore the octupole field as the particle never enters regions where the octupole field becomes significant. However, for Stormer lengths close to or less than 1.1 cm, the actual field is not as strong as predicted by the dipole approximation, and the predictions based on Stormer analysis cannot be used.

Finally, the dipole moment of the larger 5902K62 magnet is determined by the fit to be 0.4049 ± 0.0037 Am^2. The ratio of the dipole moments of the two magnets is 1.8, while the ratio of their volumes is 1.7, confirming that the dipole moment scales linearly with volume.

B.3 Estimates of Stormer Lengths

Having determined a formula for the Stormer length and the dipole moment of the deflector magnets, we can now estimate the Stormer lengths of plasma particles in the Solar Experiment. We find that, with the original magnets used on the array, electrons were assuredly deflected but that energetic ions might penetrate through the magnetic field into the array. Motivated by these results, we installed a new set of magnets into increase the Stormer length to safer values.

The typical plasma temperature on the Solar Experiment is $1 - 4$ eV [19]. We shall take the kinetic energy of the average plasma particle to be 5 eV but keep in mind that a population of

high-energy particles may be present. 5 eV corresponds to velocities of $9.4 \cdot 10^5$m/s for electrons nd $2.2 \cdot 10^4$m/s for protons, and the associated Stormer lengths for these velocities are

$$C_{\mathrm{e}} = 7.3 \text{ cm}, \tag{B.24}$$

$$C_{\mathrm{p}} = 1.1 \text{ cm}. \tag{B.25}$$

The collimator has a diameter of roughly 1.0 cm, so the Stormer length for a 5 eV electron is nearly an order of magnitude greater than the collimator diameter, and we conclude that 5 eV electrons are successfully deflected by the magnets. However, the Stormer length of a 5 eV ion is on the order of the collimator diameter. Since the field close to the magnet is weaker than a pure dipole field, we expect the Stormer length to overestimate the deflective power of the magnet near the magnet and hypothesize that the spurious signals discussed in Sec. 3.4 could be created by energetic ions streaming past the deflector magnets. Substantial populations of energetic ions might be expected in counter-helicity experiments, as anomalously high ion energies have been observed in merging spheromak experiments [23], as have fast ionic jets [118].

To eliminate the possibility of ions entering the detector, the following upgrades were made on the magnetic deflecting system. Powerful neodymium magnets were ordered; they have a remanence field of $B_r = 1.24$ T, a radius of $R = 0.79$ cm, and a height of 0.64 cm, and an estimated dipole moment of $m_d = 1.2$ A m^2 from Eq. B.16. Furthermore, two magnets were used per collimator, doubling the dipole moment. The Stormer lengths for 5 eV particles become $C_{\mathrm{e}} = 22$ cm and $C_{\mathrm{p}} = 3.3$ cm, both of which are larger than the collimating diameter. However, another major change was the geometry of the magnets in the collimator. The original magnets sat on the outer diameter of the collimator. In this setup, the height of the toroidal Stormer region would have to equal the diameter of the collimator in order to completely cover the collimator region. In the new setup, shown in Fig. (3.17), the Stormer region is now centered in the collimator, so the height of the toroidal region only has to exceed the collimator radius to entire cover the collimator interior.

Note that the Stormer length scales with particle velocity as $v^{-1/2}$ and thus with kinetic energy as $\mathrm{KE}^{-1/4}$. Thus, the Stormer length does not vary much with particle energy. Also, C scales with $m^{-1/4}$ once v has been written in terms of energy, so more massive ions penetrate further into the magnetic field. A singly charged nitrogen ion has a Stormer length that is 1.9 times smaller than a hydrogen ion of the same energy, and the Stormer length for a singly charged argon ion is 2.5 times smaller than that of a hydrogen ion of the same energy.

B.4 Deflection Near Magnets

In the region close to the magnets, the magnetic field is not as strong as that predicted by the dipole approximation, and Stormer analysis cannot be expected to hold. To determine the deflection of an energetic ion that penetrates into this region, consider an extremely energetic ion that is only slightly deflected by the magnets. Let the ion travel primarily in the x direction along the axis of the collimator, and let the magnetic field point in the z direction. The Lorentz force will deflect the ion in the y direction, and

$$m\frac{d\mathbf{v}}{dt} = qvB\hat{y}, \tag{B.26}$$

from which $d\mathbf{v} = (q/m)Bdx$, and

$$\Delta\mathbf{v} = \frac{q}{m}\int Bdx\hat{x}, \tag{B.27}$$

where the integration follows the ion trajectory through the field. In the case of slight deflection, though, we can take the trajectory to be a straight line through the collimator. The figure of merit for particle deflection is $\int Bdx$ along the path through the collimator. If $\Delta v \ll v$, then deflection angle is approximately $\Delta v/v$. We thus consider the ion deflected when

$$v \sim \Delta v = \frac{q}{m}\int Bdx\hat{x}. \tag{B.28}$$

That is, when Δv becomes of the same order as v, the ion is significantly deflected. Of course, the actual trajectory of such particles is significantly different from a straight line through the collimator, so the exact deflection cannot be easily determined, but Eq. (B.28) estimates the onset of significant deflection. To calculate this deflection parameter, the magnetic field of the upgraded deflection system was measured with a Hall probe as a function of distance into the collimator; the measurements were made as close to the collimator axis as possible with the probe aligned as nearly as possible with the axis of the magnets. These measurements are shown in the lefthand columns of Table B.1. The righthand columns tabulate Δv for each singly charged ion species up to the specified distance into the collimator and express these velocities in units of electron volts. An ion of the given species must have at least that much energy to penetrate that far into the collimator. It is thus predicted that ions would need energies of keV to penetrate through the magnetic field and reach the collimator. We note that since the deflection parameter depends on $\int Bdx$ rather than just the maximum value of B, the deflection can be improved by increasing the length of the magnetic field without necessarily increasing the maximum field strength. Longer strips of magnets could be laid along the collimator, potentially increasing $\int Bdx$ even if the maximum value of B is not as strong.

We note that, if both ions and electrons approach the collimator together, collective effects may enable the charged particles to pass the magnets even if single-particle analysis forbids each particle

Distance (mm)	Field Strength (T)	Δv_{H^+} (keV)	Δv_{N^+} (keV)	Δv_{Ar^+} (keV)
6.4	0.463	0.41	0.029	0.010
9.5	0.583	3.4	0.25	0.086
12.7	0.599	12	0.89	0.31
17.1	0.587	33	2.3	0.82
19.1	0.456	58	4.2	1.5

Table B.1: Measurements of the magnetic field as a function of distance through the collimator provide an estimate of the energies of particles needed to penetrate through the field. The right three columns give the energies of ions for which the deflection parameter $(q/m)\int Bdx$ is equal to the ion velocity at that distance into the collimator.

from passing individually. As the upgraded magnetic deflection system has successfully eliminated the spurious signals, we do not believe collective effects are in action.

Appendix C

Review of Action-Angle Variables

Action-angle variables are a useful set of phase space coordinates in Hamiltonian mechanics. The action variable is synonymous with the action integral, whose utility is discussed at length in Chapter 5. However, classical mechanics texts usually introduce action-angle variables only after a long discussion of Hamilton-Jacobi theory [92][34]. The purpose here is to introduce action-angle variables through a more direct presentation. We shall briefly review canonical transformations and generating function so that the full significance of the action-angle pair can be understood. At the end of the section, we formally demonstrate the claim made in Sec. 5.1.7 that the canonical transformation that introduces action-angle variables for the ξP_ξ variables simultaneously transforms the ηP_η pair into their averaged versions.

C.1 Canonical Transformations

We first discuss canonical transformations, a set of changes in phase space coordinates that preserve Hamilton's equations. Suppose we have a one-dimensional time-independent system $H = H(q, p)$. The equations of motion for q and p follow from Hamilton's equations:

$$\dot{q} = \frac{\partial H}{\partial p}, \tag{C.1}$$

$$\dot{p} = -\frac{\partial H}{\partial q}. \tag{C.2}$$

Suppose that we want to use a different set of coordinates QP that are some function of the old coordinates, i.e., $Q = Q(q, p)$ and $P = P(q, p)$. We then wish to determine the evolution of Q and P. One approach would be to take time derivatives of $Q = Q(q, p)$ and $P = P(q, p)$,

$$\dot{Q} = \frac{\partial Q}{\partial q}\dot{q} + \frac{\partial Q}{\partial p}\dot{p}, \tag{C.3}$$

$$\dot{P} = \frac{\partial P}{\partial q}\dot{q} + \frac{\partial P}{\partial p}\dot{p}, \tag{C.4}$$

and then substitute Eqs. (C.1) and (C.2) for $\dot{q}$ and $\dot{p}$, taking care to express q and p in terms of Q and P. This approach is guaranteed to produce the correct equations of motion for Q and P. A second tack would be to first express H in terms of Q and P: $H = H(q(Q,P), p(Q,P))$ and then invoke Hamilton's equations. This approach does *not* work, in general; that is, the equations of motion $\dot{Q} = \partial H/\partial P$ are not correct. However, there is a special subclass of transformations for which this second procedure does work, and such transformations are called canonical.

The reason why Hamilton's equations will not apply in general to the QP coordinates can be seen in the derivation of Hamilton's equation from the principle of least action, which states that small variations of system trajectories do not change the action, e.g., $\delta S = \delta \int L dt = 0$. For the canonical coordinates q and p, the Lagrangian can be written as a function of q and p through the Legendre transform: $L = p\dot{q} - H$. To derive Hamilton's equations, we set the variation of the action to zero:

$$\begin{aligned} 0 &= \delta \int_{t_1}^{t_2} \left[p\dot{q} - H(q,p)\right] dt && \text{(C.5)} \\ &= \int_{t_1}^{t_2} \left[\dot{q}\delta p + p\delta\dot{q} - \frac{\partial H}{\partial q}\delta q - \frac{\partial H}{\partial p}\delta p\right] dt && \text{(C.6)} \\ &= \int_{t_1}^{t_2} \left[\dot{q}\delta p - \dot{p}\delta q - \frac{\partial H}{\partial q}\delta q - \frac{\partial H}{\partial p}\delta p\right] dt, && \text{(C.7)} \end{aligned}$$

where the third line is derived from the second through integration by parts and from the usual assumption of no variations of the end points. Requiring that the δq and δp terms vanish independently yields Hamilton's equation. Thus, we see that Hamilton's equations are equivalent to the Lagrangian having the form $L = p\dot{q} - H$. However, when we rewrite the Lagrangian in terms of the new coordinates (Q,P), we will not, in general, obtain $P\dot{Q} - H$:

$$L = p\dot{q} - H \neq P\dot{Q} - H, \tag{C.8}$$

as can be seen by expanding the time derivative of $P\dot{Q}$:

$$P\dot{Q} = P\frac{\partial Q}{\partial q}\dot{q} + P\frac{\partial Q}{\partial p}\dot{p} \neq p\dot{q}. \tag{C.9}$$

However, the new phase space coordinates QP are canonical if one can find a so-called generating function for the transformation. We show this by exploiting a peculiar facet of the principle of least action: namely, the variation of the action $S = \int_{t_1}^{t_2} L dt$ is unchanged if we add to L the total time derivative of some other function, say F, because the contribution of F to the action,

$$\int_{t_1}^{t_2} \frac{dF}{dt} dt = \left[F(t_2) - F(t_1)\right], \tag{C.10}$$

depends only on F evaluated at the end points, and variations of the action keep the end points fixed. This function F will become the generating function used to enact canonical transforms. As discussed above, the Lagrangian L, when written in terms of QP, is different than $P\dot{Q}-H$. However, if these two quantities differ only by a total derivative, then variations of $P\dot{Q}-H$ are equivalent to variations of $L = p\dot{q} - H$, and Hamilton's equations will hold for the QP coordinates. We therefore require

$$P\dot{Q} - H(P,Q) + \frac{dF}{dt} = p\dot{q} - H(p,q). \tag{C.11}$$

If we let F have the following form,

$$F = F_1(q,P) - PQ, \tag{C.12}$$

then

$$\frac{dF}{dt} = \frac{\partial F_1}{\partial q}\dot{q} + \frac{\partial F_1}{\partial P}\dot{P} - \dot{P}Q - P\dot{Q}, \tag{C.13}$$

and using this expression in Eq. (C.11),

$$-\dot{P}Q + \frac{\partial F_1}{\partial q}\dot{q} + \frac{\partial F_1}{\partial P}\dot{P} = p\dot{q}. \tag{C.14}$$

If F_1 is chosen such that

$$Q = \frac{\partial F_1}{\partial P}, \tag{C.15}$$

$$p = \frac{\partial F_1}{\partial q}, \tag{C.16}$$

then the lefthand side of Eq. (C.14) will indeed be equal to the righthand side, and the Lagrangians will be equivalent. Equations (C.15) and (C.16) then define the transform $(q,p) \to (Q,P)$. Whenever a generating function is specified, the resulting coordinates will be canonical, and Hamilton's equations will apply.

C.2 Action-Angle Variables

We introduced the action integral $J = \oint p dq$ for periodic motion in Chapter 5, but J is only one half of a canonical set of variables called action-angle variables. The second coordinate is the angle variable ϕ, which shall be explained in this section. We will also explicitly show the generating function to obtain action-angle coordinates.

We begin by discussing the action variable. For a one-dimensional system, $H = H(q,p)$, the

action variable is

$$J(H) = \oint p(H, q) dq, \tag{C.17}$$

That is, given a trajectory of energy $H = H(q, p)$, we solve for p as a function of H and q and integrate $p(H, q)$ over q along the orbit. J is a function of H, which is a constant of motion, so J is a likewise a constant of motion. Moreover, we have, in analogy to the proof given in Sec. 5.1.2,

$$\frac{dJ}{dH} = \oint \frac{\partial p}{\partial H} dq = \oint \frac{1}{\partial H / \partial p} dq = \oint \frac{dq}{\dot{q}} = \Delta t. \tag{C.18}$$

For this one-dimensional system, the Hamiltonian H uniquely labels each trajectory by its energy. As J is a function of H, it also labels each trajectory, but this label is the phase space area enclosed by the orbit as is seen from Eq. (C.17).

If we assume that (J, ϕ) are canonical, then Hamilton's equations show that the angle coordinate ϕ essentially counts period of motion. We write the Hamiltonian H as a function of the action-angle coordinates J and ϕ by inverting the expression $J(H)$ for $H = H(J)$. Thus, H written in action-angle coordinates only depends on J and not ϕ. By Hamilton's equation, then, $\dot{J} = \partial H / \partial \phi = 0$, which confirms that J is a constant of motion. Hamilton's equation also yields $\dot{\phi}$:

$$\dot{\phi} = \frac{\partial H}{\partial J} = \frac{1}{\Delta t}. \tag{C.19}$$

Δt is itself a constant of motion, so $\dot{\phi}$ is likewise constant along a trajectory, and

$$\phi(t) = \frac{t}{\Delta t} + \phi(0). \tag{C.20}$$

At the moment when the particle has completed its nth orbit, $t = n\Delta t$ and $\phi = n + \phi(0)$, so ϕ essentially counts cycles of the trajectory. As noted by Littlejohn [119], the different orbits in phase space may have different periods, and thus particles traverse the orbits at different rates, but if the motion is parametrized by the angle variable ϕ then all particle complete a single period as ϕ approaches one.

Indeed, using (J, ϕ) as phase space coordinates has a simple analogy. Suppose we have a set of perfectly circular trajectories in the xy plane: $x = r\cos(\omega t)$ and $y = r\sin(\omega t)$. We know that these trajectories are greatly simplified by switching to polar coordinates (r, θ), for, along a circular trajectory, the radial coordinate r is constant while $\theta = \omega t$. Put another way, the r coordinate labels the particular circle, while the θ coordinate measures position along the circle. Action-angle variables are simply a generalization of this situation to non-circular curves. J is analogous to r and labels every trajectory by a geometric quantity, namely the phase space area enclosed by the curve. Similarly, ϕ, like θ, measures the location along the trajectory in terms of the fraction of time taken

to reach that point compared to the period of that orbit.

We now demonstrate a canonical transformation from (q, p) to action-angle coordinates. The appropriate generating function is

$$F_1(q, J) = \int_{q_0(J)}^{q} p(H(J), q')dq'. \tag{C.21}$$

Several points must be explained. First, since our generating function depends on J, we must write H as a function of J. Second, q_0 denotes a reference point on each trajectory from which we begin integration; the choice of q_0 is quite arbitrary and will be seen to affect the motion only in a minor fashion. This generating function is the so-called abbreviated action[1] for motion starting at q_0 up to the point q. For a complete cycle of motion, the value of the generating function is J.

We now evaluate the transformation through Eqs. (C.15) and (C.16) with J playing the role of the new momentum P and ϕ playing the role of the new coordinate Q. From Eq. (C.16),

$$p = \frac{\partial F_1}{\partial q} = p(H(J), q), \tag{C.22}$$

which simply re-expresses p as a function of q and J. Using Eq. (C.21) in Eq. (C.15) and remembering to differentiate the integral bounds, we obtain:

$$\phi = \frac{\partial F_1}{\partial J} = \int_{q_0}^{q} \frac{\partial p}{\partial H}\frac{\partial H}{\partial J}dq' + \frac{\partial q_0}{\partial J} \cdot p(H(J), q_0) \tag{C.23}$$

$$= \frac{1}{\Delta t}\int_{q_0}^{q} \frac{1}{\dot{q}}dq' + \phi_0(J), \tag{C.24}$$

where ϕ_0 is defined as

$$\phi_0 = \frac{\partial q_0}{\partial J} \cdot p(H(J), q_0). \tag{C.25}$$

Eq. (C.24) defines the angle variable ϕ. The integral in Eq. (C.24) is really just an expression for the time it takes the particle to travel from q_0 to q. Thus, ϕ evolves linearly with time and increments by unity for every period of motion, as anticipated above.

C.3 Action-Angle Transformations for Multi-Dimensional Systems

Here, we verify the claim made in Sec. 5.1.7 that, in multi-dimensional systems, the transformation of a periodic coordinate to action-angle variables simultaneously removes the periodic oscillations from the other coordinates. As in Chapter 5, we let ξ be a periodic coordinate and η be an ignorable coordinate. In this notation, the claim is that writing H as $H = H(J, P_\eta)$ rather than $H =$

[1] The action is $\int L dt = \int (p_i \dot{q}^i - H)dt$, whereas the abbreviated action is just $\int p_i \dot{q}^i dt$.

$H(\xi, P_\xi, P_\eta)$ transforms the η coordinate to an averaged version of η that evolves linearly in time at the drift velocity, and we will make this statement more rigorous by treating the substitution of J for (ξ, P_ξ) as a canonical transformation. Because J is also a function of P_η, the transformation $(\xi, P_\xi) \to (J, \phi)$ simultaneously transforms the (η, P_η) pair into a new set of coordinates, say, $(\overline{\eta}, \overline{P}_\eta)$. That is, the action-angle transformation for one pair of coordinates cannot be carried out independently of the second pair of coordinates. The situation is similar to a gauge transformation. Given the vector potential $\mathbf{A} = y\hat{x} + x^2\hat{y}$, we can enact a transformation to eliminate the x component; for instance, we can add the gradient of $\chi = -xy$ to $\mathbf{A}$. However, this simultaneously transforms the y component of the vector potential. By analogy, one cannot transform the pair $(\xi, P_\xi) \to (\phi, J)$ without also transforming $(\eta, P_\eta) \to (\overline{\eta}, \overline{P}_\eta)$. The remarkable fact about this "incidental" transformation is that $\overline{\eta}$ is the averaged version of η that evolves linearly in time at the drift velocity. One can think of $\overline{\eta}$ as an angle variable conjugate to $\overline{P}_\eta$ since its evolution is linear in time.

We develop a generating function that enacts $(\xi, P_\xi) \to (\phi, J)$. The generating function will be

$$F = S(\xi, J, \overline{\eta}, \overline{P}_\eta) - \phi J + \eta P_\eta, \tag{C.26}$$

with S to be specified shortly. Equating Lagrangians in analogy to Eq. (C.11),

$$J\dot{\phi} + \overline{P}_\eta \dot{\overline{\eta}} - H + \frac{dF}{dt} = P_\xi \dot{\xi} + P_\eta \dot{\eta} - H, \tag{C.27}$$

and expanding dF/dt gives the following transformation equations:

$$\phi = \frac{\partial S}{\partial J}, \qquad P_\xi = \frac{\partial S}{\partial \xi}, \tag{C.28}$$

$$\eta = -\frac{\partial S}{\partial P_\eta}, \qquad \overline{P}_\eta = -\frac{\partial S}{\partial \overline{\eta}}. \tag{C.29}$$

We chose S to be the abbreviated action integrated along the trajectory, $\int P_\eta d\eta + P_\xi d\xi$, in analogy to the case above. We must take care to express S as a function of $(\xi, J, \overline{\eta}, \overline{P}_\eta)$:

$$S(\xi, J, \overline{\eta}, \overline{P}_\eta) = \int_{\xi_0(J, P_\eta)}^{\xi} P_\xi \left(H(J, P_\eta), P_\eta, \xi'\right) d\xi' - \overline{\eta}\overline{P}_\eta. \tag{C.30}$$

ξ_0 is again some arbitrary function which instructs us where to begin integration along a trajectory.

We now evaluate the transformation. We have

$$\overline{P}_\eta = -\frac{\partial S}{\partial \overline{\eta}} = P_\eta, \tag{C.31}$$

so the transformation leaves the η momentum the same. We also have

$$P_\xi = \frac{\partial S}{\partial \xi} = P_\xi(H(J, P_\eta), P_\eta, \xi), \tag{C.32}$$

which is simply expressing P_ξ along a trajectory as a function of J, P_η, and ξ. The angle variable is

$$\begin{aligned}
\phi &= \frac{\partial S}{\partial J} = \int_{\xi_0}^{\xi} \frac{\partial P_\xi}{\partial H}\frac{\partial H}{\partial J} d\xi' - \frac{\partial \xi_0}{\partial J} P_\xi(H(J, P_\eta), P_\eta, \xi_0) && \text{(C.33)} \\
&= \frac{1}{\Delta t}\int_{\xi_0}^{\xi} \frac{1}{\dot{\xi}} d\xi' - \phi_0(J, P_\eta) && \text{(C.34)} \\
&= \frac{t}{\Delta t} - \phi_0(J, P_\eta), && \text{(C.35)}
\end{aligned}$$

where

$$\phi_0(J, P_\eta) = \frac{\partial \xi_0}{\partial J} P_\xi(H(J, P_\eta), P_\eta, \xi_0). \tag{C.36}$$

Again, ϕ equals the amount of time taken to reach ξ from ξ_0 divided by the period of motion. Finally, using Eq. (5.4) to evaluate $\partial H(J, P_\eta)/\partial P_\eta$, we have

$$\begin{aligned}
\eta &= -\frac{\partial S}{\partial P_\eta} = -\int_{\xi_0}^{\xi} \left[\frac{\partial P_\xi}{\partial H}\frac{\partial H(J, P_\eta)}{\partial P_\eta} + \frac{\partial P_\xi}{\partial P_\eta}\right] d\xi' - \frac{\partial \xi_0}{\partial P_\eta} P_\xi(H(J, P_\eta), P_\eta, \xi_0) + \overline{\eta} && \text{(C.37)} \\
&= -\int_{\xi_0}^{\xi} \left[\frac{1}{\dot{\xi}}\frac{\Delta\eta}{\Delta t} - \frac{\dot{\eta}}{\dot{\xi}}\right] d\xi' - \eta_0(J, P_\eta) + \overline{\eta} && \text{(C.38)} \\
&= \int_{\xi_0}^{\xi} \frac{\dot{\eta}}{\dot{\xi}} d\xi' - \frac{\Delta\eta}{\Delta t} t - \eta_0(J, P_\eta) + \overline{\eta}, && \text{(C.39)}
\end{aligned}$$

where

$$\eta_0(J, P_\eta) = \frac{\partial \xi_0}{\partial P_\eta} P_\xi(H(J, P_\eta), P_\eta, \xi_0). \tag{C.40}$$

The integral evaluates to η, and canceling η from both sides of Eq. (C.39) gives

$$\overline{\eta} = \frac{\Delta\eta}{\Delta t} t + \eta_0(J, P_\eta). \tag{C.41}$$

This shows that $\overline{\eta}$ evolves linearly in time at the drift velocity $\Delta\eta/\Delta t$. This fact was derived as consequence of effecting a transformation to action-angle coordinates for the (ξ, P_ξ) pair.

Appendix D

Additional Calculations

The following sections contain several calculations that can be omitted from Chapter 5 on a first read but that may be of interest to those desiring more detail.

D.1 First-Order Correction and Guiding Center Definitions

In Sec. 5.2.4, we retained the first-order term in the expansion of the potential V and obtained

$$J(H, P_y) = J_0 \left(H - qV(x_{\rm gc}, y, t) + \frac{m}{2} \left(\frac{\partial_x V}{B_z} \right)^2 , \ P_y \right), \tag{D.1}$$

where J_0 is the action integral when $V = 0$. We observed that the effects of retaining the δx term of V is to add to the energy the term $(m/2)(\partial_x V/B)^2$, which leads to a higher-order correction to the drift velocity shown in Eq. (5.147). However, we shall now see that this terms can be viewed as a consequence of the the definition of guiding center. We highlight this fact because any comparison of higher-order drifts derived in Ch. 5 with other work on guiding center drifts needs to take into account the possibility of a discrepancy guiding center definitions.

We defined the guiding center as the x location where the y velocity vanished. In Sec. 5.2.1, this definition was consistent with the fact that the guiding center approximation is a harmonic-oscillator approximation because $x_{\rm gc}$ is the minimum of the effective potential

$$U_{\rm eff} = \frac{(P_y - qA_y)^2}{2m}. \tag{D.2}$$

In Sec. 5.2.4, we continued to use this definition of guiding center even after introducing the potential V. However, the effective potential is now different:

$$U_{\rm eff} = \frac{(P_y - qA_y)^2}{2m} + qV, \tag{D.3}$$

so that $x_{\rm gc}$, as previously defined, is no longer the minimum of $U_{\rm eff}$.

If we assume that the electric field is a perturbation to the problem of a charged particle in a magnetic field, then we expect that the true location of the minimum, which we will denote x_m, is not very different from $x_{\rm gc}$, that is, $x_m = x_{\rm gc} + \delta x_{\rm gc}$, where $\delta x_{\rm gc}$ is assumed small. We determine $\delta x_{\rm gc}$ by requiring that x_m minimizes $U_{\rm eff}$:

$$0 = \left.\frac{dU_{\rm eff}}{dx}\right|_{x=x_m} = \left[-qB_z\frac{P_y - qA_y}{m} + q\frac{dV}{dx}\right]_{x=x_m}. \tag{D.4}$$

We do a Taylor expansion about $x_{\rm gc}$

$$0 = -q\left(B_z(x_{\rm gc}) + \frac{dB_z}{dx}(x_{\rm gc})\delta x_{\rm gc}\right)\frac{P_y - qA_y(x_{\rm gc}) - qB_z(x_{\rm gc})\delta x_{\rm gc}}{m} + q\frac{dV}{dx} + q\frac{d^2V}{dx^2}\delta x_{\rm gc}, \tag{D.5}$$

where all derivatives are evaluated at $x_{\rm gc}$. We now recall that, by definition, $P_y = qAy(x_{\rm gc})$ (see Eq. (5.90)), so, keeping terms up to first order in $\delta x_{\rm gc}$,

$$0 = \frac{q^2}{m}B_z^2\delta x_{\rm gc} + q\frac{dV}{dx} + q\frac{d^2V}{dx^2}\delta x_{\rm gc}. \tag{D.6}$$

Solving for $\delta x_{\rm gc}$,

$$\delta x_{\rm gc} = -\frac{\partial_x V}{qB_z^2/m + \partial_{xx}V}. \tag{D.7}$$

In the case where the second derivative of V is small enough to be dropped, we would have $\delta x_{\rm gc} = -m\partial_x V/qB_z^2$.

We now show that the corrected drift velocity in Eq. (5.148) is actually the value of the $\mathbf{E}\times\mathbf{B}$ velocity evaluated at x_m rather than $x_{\rm gc}$. Indeed,

$$\begin{aligned}
\frac{\mathbf{E}(x_m)\times\mathbf{B}(x_m)}{B^2(x_m)} &= \frac{\partial_x V(x_m)}{B_z(x_m)} && \text{(D.8)}\\
&\approx \frac{\partial_x V(x_{\rm gc})}{B_z(x_{\rm gc})} + \delta x_{\rm gc}\frac{d}{dx}\left[\frac{\partial_x V}{B_z}\right]_{x=x_{\rm gc}} && \text{(D.9)}\\
&= \frac{\partial_x V(x_{\rm gc})}{B_z(x_{\rm gc})} - \frac{m\partial_x V}{qB_z^2}\frac{d}{dx}\left[\frac{\partial_x V}{B_z}\right]_{x=x_{\rm gc}} && \text{(D.10)}\\
&= \frac{\partial_x V(x_{\rm gc})}{B_z(x_{\rm gc})} - v_{E\times B}\frac{m}{qB_z}\frac{d}{dx}\left[\frac{\partial_x V}{B_z}\right]_{x=x_{\rm gc}}. && \text{(D.11)}
\end{aligned}$$

Hence, the higher-order term term in Eq. (5.148) can be viewed as a correction to the $\mathbf{E}\times\mathbf{B}$ that corrects for the fact that the $\mathbf{E}\times\mathbf{B}$ was evaluated at $x_{\rm gc}$ rather than x_m.

D.2 Cyclotron-Driven Pondermotive-Potential

In Eq. (5.138), the energy is modified by the addition of the term $(m/2)(\partial_x V/B)^2$. Here, we show that this added term is a pondermotive-like potential that arises due to the cyclotron motion.

Pondermotive potentials arise when a charged particle is placed in an oscillating electric field when the field amplitude varies with position. By averaging the equation of motion for the charged particle, it is seen that there is a effective force that drives the particle away from the large field regions and that this force can be described by an effective pondermotive potential [120]:

$$U_{\text{pon}} = \frac{q^2 E(x)^2}{4m(\omega - \mathbf{k}\cdot\mathbf{v})}. \tag{D.12}$$

ω is the wave frequency, $\mathbf{k}$ is the wave vector of the wave generating the electric field, and $\mathbf{v}$ is the averaged velocity of the charged particle. For a particle in a crossed electric and magnetic field, there are no waves, but the particle *experiences* an oscillating electric field due to the cyclotron motion. We take Eq. (D.12) and set $\mathbf{k} = 0$, since we are not dealing with a wave, and set $\omega = qB_z/m$, the cyclotron frequency. Since the oscillations are in the x direction, we use $E = E_x = -\partial_x V$. Then Eq. (D.12) becomes

$$U_{\text{pon}} = \frac{q^2(\partial_x V)^2}{4m(qB_z/m)} = \frac{m}{4}\left(\frac{\partial_x V}{B_z}\right)^2, \tag{D.13}$$

which equals the added term in Eq. (5.138) up to a factor of two. This factor of two can be explained as follows. In the wave case, the particle experiences a sinusoidal electric field, but in the cyclotron-driven case the particle experiences a square-wave-like $\mathbf{E}$. The E that appears in Eq. (D.12) is the field amplitude of a sinusoidal field; if we rewrite Eq. (D.12) in terms of the root mean square of the field, we would have

$$U_{\text{pon}} = \frac{q^2(2E_{\text{RMS}}(x))^2}{4m(\omega - \mathbf{k}\cdot\mathbf{v})}, \tag{D.14}$$

in which case Eq. (D.13) is

$$U_{\text{pon}} = \frac{m}{2}\left(\frac{E_{\text{RMS}}}{B_z}\right)^2. \tag{D.15}$$

Since, in the cyclotron-driven case, $E_{\text{RMS}} = E = \partial_x V$, Eq. (D.15) is precisely the extra potential term in Eq. (5.138).

D.3 A Lemma on Averaging

We develop a lemma concerning the averaging of a scalar function $f(x)$ over a gyro-orbit again for the case of a magnetic field $\mathbf{B} = B_z(x)\hat{z}$. Let the average of $f(x)$ be defined as

$$\bar{f} = \frac{\int_{t_0}^{t_0+\Delta t} f(x(t))dt}{\Delta t}, \tag{D.16}$$

and define $\delta x = x - x_{\text{gc}}$. Using Eq. (5.91), we can relate δx to $\dot{y}$:

$$m\dot{y}(x) \quad = \quad P_y - qA_y(x_{\text{gc}} + \delta x) \tag{D.17}$$

$$\approx \quad P_y - qA_y(x_{\rm gc}) - q\left.\frac{dA_y}{dx}\right|_{x_{\rm gc}} \delta x \tag{D.18}$$

$$= \quad qB_z(x_{\rm gc})\delta x. \tag{D.19}$$

We exploit Eq. (D.19) in a Taylor expansion $f(x)$ so that the average of f becomes

$$\bar{f} = \frac{1}{\Delta t}\int_{t_0}^{t_0+\Delta t}\left[f(x_{\rm gc}) + \frac{f'(x_{\rm gc})}{qB_z(x_{\rm gc})} m\dot{y}(x)\right] dt \tag{D.20}$$

$$= f(x_{\rm gc}) + \frac{m}{qB_z(x_{\rm gc})} f'(x_{\rm gc}) v_d, \tag{D.21}$$

where $v_d = \Delta y/\Delta t$ is the drift velocity in the y direction. The second term is a correction term which involves the y drift. Because $m/qB_z = \Delta t/2\pi$, we also have

$$\bar{f} = f(x_{\rm gc}) + \frac{1}{2\pi} f'(x_{\rm gc})\Delta y, \tag{D.22}$$

and it is interesting to note that the correction involve an x derivative of f times the net y displacement.

D.4 Flux Enclosed by an Orbit: Lab Frame Calculation

In this section, we rederive the magnetic flux enclosed by one gyration of a charged particle in a magnetic field through a different technique than that presented in Sec. 5.2.5. In the lab frame, the flux is not well-defined because the trajectory does not close on itself, so we do not have a definite surface through which to compute flux. We surmount this difficulty by artificially closing the trajectory, computing the flux, and then judicious averaging the answer over a period of motion. The flux obtained is equal to that given in Eq. (D.26). For clarity, we shall work with magnetic fields $\mathbf{B} = B_z(x)\hat{z}$ so that the only drift is the grad-B drift, which is in the y direction.

While the trajectory does not close on itself, we can define a flux value for each point along the trajectory. Given a point (x_0, y_0) on the trajectory, the regions through which we will measure flux are bounded by two curves defined as follows. The first curve follows the trajectory for one period as the particle moves from (x_0, y_0) to $(x_0, y_0 + \Delta y)$. The second curve is a vertical segment of length Δy that joins the starting point with the endpoint. Fig. D.1 shows several such regions for different starting locations; it is apparent that every region encloses a different amount of flux.

We now evaluate the flux, which we denote by $\Phi(x_0)$, through each region defined above for a point (x_0, y_0). The surface integral for flux can, by Stokes' theorem, be converted into a line integral of $\mathbf{A}$, and this line integral is split into two parts: the segment that follows the trajectory and the

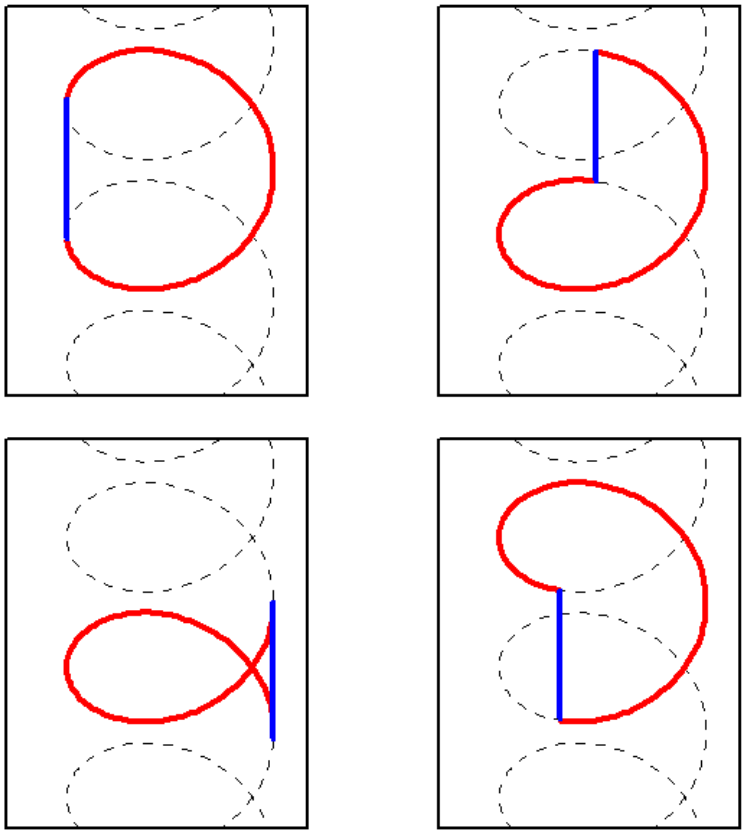

Figure D.1: In the lab frame, the flux of a gyration depends on how one defines the starting point; this figure explicitly shows four possibilities. The dotted lines represents an electron trajectory, and the solid red and blue lines together bound the region through which we measure flux. The solid red lines trace one period of motion, while the solid blue lines are the connecting paths used to close the gyro-orbits. Clearly, the amount of flux enclosed is different for each region.

vertical segment that joins the starting and ending points.

$$\Phi(x_0) \quad = \quad \oint \mathbf{A} \cdot d\mathbf{l} = \int_{\text{trajectory}} \mathbf{A} \cdot d\mathbf{l} + \int_{\text{connecting}} \mathbf{A} \cdot d\mathbf{l}, \tag{D.23}$$

The first integral is equal to $\partial J/\partial q$ by virtue of Eq. (5.160) with $V = 0$. Therefore

$$\Phi(x_0) \quad = \quad \frac{\partial J}{\partial q} - A_y(x_0)\Delta y. \tag{D.24}$$

The first term is the contribution from the trajectory itself and is independent of x_0. The second term comes from the connecting path and clearly depends upon x_0. This x_0 dependence is undesirable, for we would like flux to be a property of the entire orbit just as the area of a geometric shape has nothing to do with any particular point along the perimeter.

To obtain a flux that is independent of starting point and representative of the entire orbit, we

take the democratic approach and average $\Phi(x_0)$ over all points on a trajectory. The averaging will be weighted by the amount of time the particle in orbit spends at position x_0, just as in Eq. (D.16). $A_y(x)$ is easily averaged by considering $P_y = mv_y + qA_y(x)$ and observing that the average of v_y is the drift velocity $v_d = \Delta y/\Delta t$, from which

$$\bar{A}_y = \frac{1}{q}\left(P_y - m\frac{\Delta y}{\Delta t}\right). \tag{D.25}$$

Strangely, this is the same answer as would have been obtained from the approximate averaging formula given by Eq. (D.22), which apparently holds exactly for the function $A_y(x)$. Substituting $\bar{A}_y$ from Eq. (D.25) into Eq. (D.24) gives

$$\Phi = \frac{\int \Phi(x(t))dt}{\Delta t} = \frac{\partial J}{\partial q} - \frac{1}{q}\left(P_y - m\frac{\Delta y}{\Delta t}\right)\Delta y. \tag{D.26}$$

This result will be verified in the following section, where we will evaluate the flux by a different technique.

D.5 Phase Space Contours

We rederive Eq. (5.168) by integrating over special phase space contours using techniques from differential geometry as described by Montgomery [103]. The contours lie entirely within the submanifolds of phase space defined such that P_y is constant. Such submanifolds have three dimensions with coordinates (x, P_x, y). The contours consist of two parts: the first part follows the trajectory over one gyration, while the second part travels in the y direction to rejoin its starting point. Fig. D.2 depicts such a contour. The contours used in Sec. D.4 to compute the flux are the projections of these contours onto the xy plane.

The proper way of proceeding would be to invoke techniques from differential geometry [94, pg. 174]. Differential geometry generalizes concepts from multivariate calculus to manifolds of arbitrary dimensions, and these generalizations often do not require a metric, or definition of distance, on the manifold. Phase space, for example, is an abstract space in which we cannot talk about notions of distance, but differential geometry allows us to talk about integrals over lines and surfaces. Fortunately, the manifolds we will consider have three dimensions, and this allows us to identify techniques from differential geometry with those from three-dimensional calculus. For instance, a one-form is a mathematical object from differential geometry that is integrated over lines, and a two-form is integrated over two-dimensional surface. On a three-dimensional manifold, however, these are analogous to line and surface integrals of vector fields. Montgomery provides a very readable explanation of differential forms in this context.

With that preamble, we integrate the canonical one-form, also known as Poincare's form [94, pg.

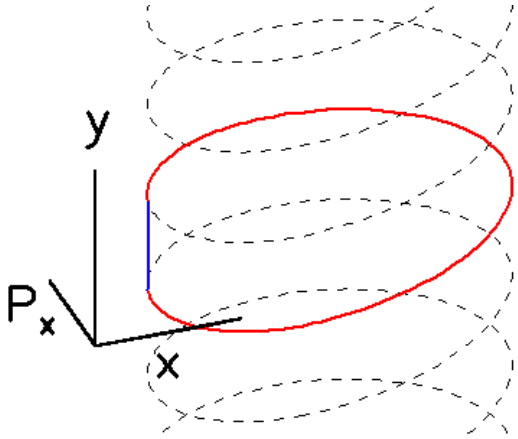

Figure D.2: The phase space contour under consideration follows the trajectory for one period, as shown by the red line, and then rejoins its starting point by traveling straight up the y axis, as shown by the blue line.

238], over the contours discussed above. The canonical one-form is

$$\theta = P_x dx + P_y dy, \tag{D.27}$$

but we can identify θ with a phase space vector field $\mathbf{V}$:

$$\mathbf{V} = P_x \hat{x} + P_y \hat{y}. \tag{D.28}$$

We now perform the integration. Over the first part of the contour, kinetic energy is constant, so

$$\begin{aligned} \int_I \theta &= \int_I \mathbf{V} \cdot d\mathbf{l} && \text{(D.29)} \\ &= \int_I [m v_x dx + m v_y dy + qA(x) dy] && \text{(D.30)} \\ &= \int_I m \left[v_x^2 + v_y^2\right] dt + q \int_I A(x) dy && \text{(D.31)} \\ &= 2H\Delta t + q \frac{\partial J}{\partial q}. && \text{(D.32)} \end{aligned}$$

Integrating over the second branch,

$$\int_{II} \theta = \int_{II} \mathbf{V} \cdot d\mathbf{l} = \int_{II} P_y dy = -P_y \Delta y. \tag{D.33}$$

The minus sign occurs because we are traveling backwards in the sense opposite to Δy. Since the total contour is closed, we apply Stokes' theorem. In differential geometry, we would take the differential of θ and obtain the two-form $d\theta = dP_x \wedge dx$, since P_y is constant on the submanifold. Thinking in terms of vector calculus, taking the differential of θ is equivalent to taking the curl of

$\mathbf{V}$, $\nabla \times \mathbf{V} = \hat{y}$. Either way, we integrate over the surface spanned by the contour:

$$\int_{I+II} \mathbf{V} \cdot d\mathbf{l} = \int \nabla \times \mathbf{V} \cdot d\mathbf{S} = \int \hat{y} \cdot d\mathbf{S} = J(H, P_z), \tag{D.34}$$

because $\hat{y} \cdot d\mathbf{S}$ is the project of the area element onto the xP_x plane, and this area is indeed the x action. Equating the line integral, which is the sum of Eqs. (D.32) and (D.33), with the surface integral given by Eq. (D.34), gives

$$J(H, P_y, q) = 2H\Delta t + q\frac{\partial J}{\partial q} + P_y \frac{\partial J}{\partial P_y}. \tag{D.35}$$

which is equivalent to Eq. (5.168).